

**SILICON QUANTUM DOTS DERIVED FROM
ZINC OXIDE INCORPORATED POROUS
SILICON FOR PHOTOVOLTAIC APPLICATIONS**

MOHAMMAD SAMIR ALI ALMOMANI

UNIVERSITI SAINS MALAYSIA

2022

**SILICON QUANTUM DOTS DERIVED FROM
ZINC OXIDE INCORPORATED POROUS
SILICON FOR PHOTOVOLTAIC APPLICATIONS**

by

MOHAMMAD SAMIR ALI ALMOMANI

**Thesis submitted in fulfilment of the requirements
for the degree of
Doctor of Philosophy**

April 2022

Dedication

This research is dedicated to the

**NABI MOHAMMAD ﷺ BIN ABDULLAH BIN ABDUL MUTTALIB,
HIS FAMILY, AND FRIENDS.**

ACKNOWLEDGEMENT

Thank you, Almighty Allah, for providing me with the energy and courage to complete this research. I accept that it is only by His Goodness and Wisdom that I have progressed this far in my educational goals.

I would like to give special thanks to several people who contributed to the success of our project. First, I would like to thank my main supervisor Dr. Naser Mahmoud Ahmed, for his courage, advice, support, helpful directions, academic and financial inspiration throughout the research process, and encouragement that played a significant role in completing this thesis. I would like also thankful to my co-supervisor Dr. Mohd Marzaini Bin Mohd Rashid, for his careful consideration and motivation throughout the project's duration. Finally, I would like to express my gratitude to the academic and non-academic employees at USM's School of Physics for their help and support in this study.

My parents, Samir Ali Almomani and Um Mohammad Almomani have received special recognition for their trust, support, and prayer for us. I am grateful to my uncle Talal Mahameed and aunt Um Ammar for their confidence, and support. In addition, I appreciate and thankfully my family, my wife Um Obadah, my kids Obadah and Orjwan for their patience, endurance, trust, support, and prayer to me. Thank you to all of my family members, research partners, friends, and everyone else who helped and supported me during this project session will be remembered.

MOHAMMAD ALMOMANI 2022

TABLE OF CONTENTS

ACKNOWLEDGEMENT	ii
TABLE OF CONTENTS	iii
LIST OF TABLES	viii
LIST OF FIGURES	x
LIST OF SYMBOLS	xvii
LIST OF ABBREVIATIONS	xviii
ABSTRAK	xxii
ABSTRACT	xxiv
CHAPTER 1 INTRODUCTION	1
1.1 Overview	1
1.2 Background of Graded Bandgap Solar Cells	2
1.3 Problem Statement	5
1.4 Objectives.....	7
1.5 Hypothesis.....	8
1.6 Scope of Study	8
1.7 The Originality of the Study.....	9
1.8 Thesis Outline	9
CHAPTER 2 LITERATURE REVIEW	11
2.1 Material Classification	11
2.2 Dopants-Based Classification	12
2.3 Energy Band Origination	14
2.4 Band Symmetry-Based Classification.....	15
2.5 Porous Silicon	17
2.5.1 Overview	17
2.5.2 Mechanism of Electrochemical Etching	18

2.5.3	Electrochemical Etching	19
2.5.3(a)	Etching Current Density	20
2.5.3(b)	Hydrofluoric Acid Concentration.....	21
2.5.3(c)	Etching Time	21
2.5.4	Photoluminescence of the Porous Silicon	22
2.5.4(a)	Nanosize Silicon-Established Model.....	23
2.5.4(b)	Silicon Hydrogen-Established Model.....	24
2.5.4(c)	Silicon Oxide -Established Model.....	25
2.5.5	Enhancement of the Porous Silicon Properties by Organic and Inorganic Materials	25
2.6	Silicon Quantum Dots Properties	29
2.6.1	Silicon Quantum Dots and Quantum Confinement Effect.....	29
2.6.2	Preparing Silicon Quantum Dots and Photoluminescence Properties.....	33
2.7	Titanium Dioxide	37
2.7.1	Titanium Dioxide Nanoparticles for Photovoltaic Devices	37
2.8	Junctions and Interfaces of Solar Cells	38
2.8.1	p-n Junction.....	38
2.8.2	p-i-n Junction.....	39
2.8.3	Metal- Semiconductor Junction	40
2.8.3(a)	Ohmic Contact.....	41
2.8.3(b)	Rectifying (Schottky) Contacts.....	42
2.8.4	Interfaces of Metal-Insulator-Semiconductor	43
2.9	Types of Solar Cells and Working Principle.....	44
2.9.1	Crystalline Silicon Cells: First-Generation PV Technologies	45
2.9.2	Thin-Film solar cells: Second Generation Photovoltaic Technologies	47
2.9.3	Third Generation Solar Cells.....	48

2.9.3(a)	Dye-Sensitized Solar Cells	48
2.9.3(b)	Organic Solar Cells.....	48
2.9.3(c)	Perovskites PVs	49
2.9.3(d)	Kesterite Solar Cells	50
2.9.3(e)	Quantum Dots Solar Cells	50
2.9.4	Utilising Quantum Dots in Solar Cells.....	51
2.9.4(a)	Silicon Quantum Dots for Polymer Solar Cells.....	55
2.9.4(b)	Silicon Quantum Dots for Heterojunction Solar Cells	56
2.9.4(c)	Silicon Quantum Dots for Quantum Dots sensitized Solar Cell	57
CHAPTER 3	METHODOLOGY.....	60
3.1	Materials.....	61
3.2	Synthesis of Zinc/Porous Silicon and Zinc/Silicon Quantum Dots at Different Parameters by a Top-Down Process.....	61
3.2.1	Electrochemical Etching Cells	63
3.3	Synthesis of Zinc/Silicon Quantum dots by a Bottom-Up Process.....	64
3.4	Preparation of Titanium dioxide Nanoparticles by Spray Pyrolysis Process.	65
3.5	Solar Cells Fabrication	66
3.5.1	Synthesis of Porous Silicon Layers for Solar Cells.....	66
3.5.2	Synthesis of the Graded Bandgap Quantum Dots Solar Cells	67
3.6	List of Equipments	68
3.6.1	Radio Frequency and Direct Current Sputtering Magnetron Sputtering	68
3.6.2	Spin Coating.....	69
3.6.3	Ultraviolet-Visible Spectroscopy	70
3.6.4	Fourier Transform Infrared Spectrometer System	70
3.6.5	Field-Emission Scanning Electron Microscope	71
3.6.6	Transmission Electron Microscope	72

3.6.7	Atomic Force Microscopy.....	73
3.6.8	High-Resolution X-Ray Diffractometer System	74
3.6.9	Photoluminescence (PL) Test	76
3.6.10	X-ray Photoelectron Spectroscopy.....	76
3.6.11	The Electrical Circuit Measurement System	77
CHAPTER 4	RESULTS AND DISCUSSION.....	79
4.1	Etching Parameters.....	79
4.1.1	Current Density and Mechanism of the Pores formation.....	79
4.1.1(a)	Physical Properties.....	80
4.1.1(b)	Optical Properties	86
4.1.2	Zinc Mass Effect on the Zn/Porous Silicon Properties	88
4.1.2(a)	Morphology and Surface Characterization.....	88
4.1.2(b)	Optical Properties	93
4.1.3	Etching Time-Dependent Optical Properties of Zinc/Porous Silicon.....	97
4.1.4	Hydrofluoric Acid Concentration-Dependent Structural and Optical Properties of Zinc/Porous Silicon.....	99
4.2	Zinc/Silicon Quantum Dots: Preparation and Characterization.....	101
4.2.1	Preparing Zinc/Silicon Quantum Dots by a Top-Down Process	101
4.2.1(a)	Morphological Analysis.....	102
4.2.1(b)	Optical Properties	105
4.3	Regrowth Zinc/Silicon Quantum Dots via the Bottom-Up Process.....	110
4.3.1	Structural Characteristics of Zinc/Silicon Quantum Dots.....	110
4.3.2	Optical Characteristics of Zinc/Silicon Quantum Dots After Regrowth	112
4.3.3	Mechanism of Zinc/Silicon Quantum Dots Regrowing.....	120
4.4	Titanium Dioxide Nanoparticles Properties	122
4.4.1	Morphology, Structure and Optical Properties of Samples.....	122

CHAPTER 5	GRADED BANDGAP SOLAR CELLS.....	131
5.1	Porous Silicon Layer Properties	131
5.1.1	Morphology and Optical Characteristics of Porous Silicon.....	131
5.1.2	Effect of Porous Silicon on Performance of Solar Cells.....	140
5.2	Effect of Titanium Dioxide Nanoparticles on the Performance of the Solar Cells.....	142
5.3	Effect of Deposit Single Layer of ZnSi Quantum Dots (SL-ZnOSi QDs) with Unified size on the Performance of the Solar Cells	148
5.4	Effect of Deposited Zinc Silicon Quantum Dots Double and Triple Layers (DL-ZnOSi QDs and TL-ZnOSi QDs) on Cell's Performance.....	152
CHAPTER 6	CONCLUSION AND FUTURE WORKS	162
6.1	Conclusions	162
6.2	Prospects for Future Works.....	163
REFERENCES.....		165
LIST OF PUBLICATIONS		

LIST OF TABLES

	Page
Table 2.1	The list of essential qualities of various solid-state materials [24]. ... 11
Table 2.2	Lists of semiconductor elements and compounds used in PV devices are provided below [24]. 14
Table 2.3	Achieved FWHM and enhancement factor of the PL peak intensity of the present work compared to the state-of-the-art in other reports in the literature on PSi structures containing different metals, metal oxide, semiconductors, and polymers. 28
Table 2.4	Summary of PCE of Si QDs for different types of solar cells. 58
Table 2.5	Performance parameters comparison of the studied solar cells. 59
Table 4.1	The porosity and thickness measurements of the PSi (n-type Si) by gravity method. 81
Table 4.2	Percentage distribution of Zn on the PSi surface at different positions obtained via EDX spectral analysis. 91
Table 4.3	Emission peak wavelength, enhancement factor, and FWHM of the synthesised Zn PSi. 95
Table 4.4	Zn content-dependent PL peak wavelength, enhancement factor, FWHM (nm), bandgap energy, and porosity of the synthesised ZnPS. 97
Table 4.5	Etching time-dependent optical properties of the PSi without and with Zn (0.17 g) incorporation. 99
Table 4.6	Dependence of the emission peak wavelength (λ_{peak}) and the corresponding spectral full width at half the maximum ZnOSi QDs on the variation of the NH_4OH content. 118
Table 4.7	Dependence of the emission peak wavelength and the corresponding spectral full width at half-maximum ZnOSi QDs on the excitation wavelength changes. 120

Table 5.1	Performance solar cell structure of Al/p-c-Si/PSi/Ag at different etching time.....	141
Table 5.2	Comparative evaluation of the performance of the proposed cell with other state-of-the-art works reported in the literature.	148
Table 5.3	Performance parameter of the solar cell of Al/p-c-Si/PSi/ TiO ₂ NPs/Ag; Al/p-c-Si/PSi/ZnOSi QDs (7.4 nm) / TiO ₂ NPs /Ag; Al/p-c-Si/PSi/ZnOSi QDs(2.7 nm)/TiO ₂ NPs /Ag; and Al/p-c-Si/PSi/ZnOSi QDs (2.1 nm) /TiO ₂ NPs /Ag	151
Table 5.4	Performance parameters comparison of the studied solar cells	160
Table 5.5	Performance parameters comparison of the studied solar cells.	161

LIST OF FIGURES

		Page
Figure 1.1	An energy band diagram showing the major energy lack pathways: (1) recombination loss; (2,3, and 4) thermalization loss ; (5) photons with insufficient energy cause non-absorption.....	1
Figure 1.2	Diagram of GBGSCs [5].....	4
Figure 2.1	An intrinsic semiconductor's energy band diagram.	13
Figure 2.2	Electronic structures of Si-doped with (a) boron and (b) phosphorus.	13
Figure 2.3	Energy band diagram of (a) p-type and (b) n-type semiconductor. ...	14
Figure 2.4	(a) Direct and (b) indirect bandgap semiconductor.....	16
Figure 2.5	Si energy band models in HF electrolyte: (a) and (c) are p and n-Si, respectively at equilibrium condition, (b) and (d) are p and n-type Si with a positive bias voltage (+).....	19
Figure 2.6	Schematic depiction of how the bulk change to the QDs impacts the CB, VB levels and E_g in Si QDs.	32
Figure 2.7	(a) and (b) are p-type and n-type semiconductors before and after p-n junction generation, respectively (c) Energy band schematics of p-type and n -type semiconductors before and after p-n junction generation and (d) band bending of the p-n junction after creation.	39
Figure 2.8	A p-i-n junction energy band diagram.	40
Figure 2.9	(a) and (b) are before and after M/p-type ohmic contact, respectively, (c) and (d) are after M/n-type ohmic contact, respectively.	41
Figure 2.10	(a) and (b) are before and after M/n-type-S Schottky contact, respectively, (c) and (d) are after M/p-type-S Schottky contact, respectively.	43

Figure 2.11	An MIS interface energy band diagram increases potential Φ_b due to a thin insulating layer at the interface.	44
Figure 2.12	Solar radiation spectrum [146].....	44
Figure 2.13	Effect of air mass on solar radiation [148].....	45
Figure 2.14	The basic structure of the c-Si solar cell (p-n junction) is depicted schematically.....	46
Figure 2.15	Schematic diagram of the mechanism in an OSCs.	49
Figure 2.16	Schematic illustration of energy transfer from Si QD to n-Si [170].	54
Figure 3.1	Flowchart of preparation Zn PSi and ZnOSi QDs.	60
Figure 3.2	A schematic diagram of (a) single and (b) ring cells utilised for electrochemical etching.....	64
Figure 3.3	(a) Flowchart of the TiO ₂ NPs preparation procedure, and (b) TiO ₂ thin films deposition procedure.....	66
Figure 3.4	Auto HHV500 sputter coater.	68
Figure 3.5	Spin coating device.	69
Figure 3.6	UV-Vis equipment.....	70
Figure 3.7	FTIR equipment.....	71
Figure 3.8	FESEM equipment.	72
Figure 3.9	TEM equipment.	73
Figure 3.10	AFM equipment.....	74
Figure 3.11	HR-XRD equipment.....	75
Figure 3.12	The PL system.	76
Figure 3.13	The image of the solar simulator.	78
Figure 4.1	FESEM images of the Zn PSi derived from n-Si at various current densities (a) 5 mA/cm ² , (b) 15 mA/cm ² , (c) 20 mA/cm ² (d) 30 mA/cm ² , and (e) 40 mA/cm ²	83

Figure 4.2	XRD analysis of Zn PSi at various current densities of (a) 0 mA/cm ² , (b) 5 mA/cm ² , (c) 10 mA/cm ² , (d) 20 mA/cm ² , and (e) 30 mA/cm ² , (f) summary of relation between etching current density with the crystallite size and FWHM.....	85
Figure 4.3	FTIR of PSi with and without additive Zn.....	85
Figure 4.4	PL of the Zn PSi etched at (a) 5 mA/cm ² , (b) 15 mA/cm ² , (c) 20 mA/cm ² , (d) 30 mA/cm ²	87
Figure 4.5	The relation between etching current density versus the bandgap and porosity.....	88
Figure 4.6	FESEM images (top view) of the prepared PSi with (a) 0 g (pure or undoped), (b) 0.11 g, (c) 0.17 g, and (d) 0.25 g of added Zn.	89
Figure 4.7	Variation in the porosity of the Zn PSi.	89
Figure 4.8	XRD of the Zn PSi with various Zn mass.....	90
Figure 4.9	FESEM images (cross-section view) of the prepared Zn PSi with 0.17 g of included Zn at different positions in the PS channel.	92
Figure 4.10	XPS spectra of the prepared Zn PSi for the Si2p, O1s, and Zn2p states.....	93
Figure 4.11	Emission spectra (HPC-2 collimated light source (λ_{exc} 365 nm)) of the prepared Zn PSi (a) without and with (b) 0.11 g, (c) 0.17 g, and (d) 0.25 g of included Zn.....	94
Figure 4.12	PL spectra of the prepared Zn PSi under excitation wavelength of 325 nm (a) without (pure or undoped) and with (b) 0.11 g, (c) 0.17 g, and (d) 0.25 g of included Zn.....	96
Figure 4.13	Emission spectra of the Zn PSi samples prepared at the etching time of (a) 20 minutes without Zn, and the etching times of (b) 15 minutes, (c) 20 minutes, and (d) 30 minutes with 0.17 g of Zn.	98
Figure 4.14	FESEM morphology of the PSi etched at (a) 1:7, (b) 3:7, (c) 5:7, and (d) 7:7.	101
Figure 4.15	Visible fluorescence under 365 nm from the (a) Zn PSi-1:7 (b) Zn PSi-7:1. (c) and (d) are suspended of ZnOSi QDs-1:7, ZnOSi QDs-	

	7:1 under 365 nm and 425 nm, respectively. (e) ZnOSi QDs-7:1 and (f) ZnOSi QDs-1:7 are 390 nm.....	102
Figure 4.16	The FESEM images the (a) cross-sectional of the ZnOSi QDs-7:1 and (b) ZnOSi QDs-1:7, (c) top view of the ZnOSi QDs-7:1, (d) ZnOSi QDs-1:7 and (e) EDX of the ZnOSi QDs-1:7	104
Figure 4.17	The EFTEM images of (a) ZnOSi QDs-7:1 and (b) ZnOSi QDs-1:7.....	104
Figure 4.18	The UV-Vis-NIR absorption spectrum of the (a) ZnOSi QDs-7:1 and (b) ZnOSi QDs-1:7. Inset: Tauc plot for the bandgap estimation.	106
Figure 4.19	Emission spectrum of the ZnOSi QDs-7:1 and ZnOSi QDs-1:7 excited under (a) 365 nm, (b) 390 nm, and (c) 425 nm. In each Figure shows the visible fluorescence observed by naked eyes.	107
Figure 4.20	(a-d) EFTEM images of the colloidal ZnSiQD suspension in acetone prepared with NH ₄ OH of 0, 15, 20, and 25 μ L, respectively. (a ₁ -d ₁) particle size distributions of the colloidal ZnOSi QDs (20 mL) suspended in acetone with NH ₄ OH of 0, 15, 20, and 25 mL, respectively. (e) NH ₄ OH: 25 μ L high resolution. ..	112
Figure 4.21	Luminescence from colloidal ZnOSi QDs containing various amounts of NH ₄ OH under different excitation wavelengths.	114
Figure 4.22	ZnSiQD suspension in acetone prepared (a) without and (b) with NH ₄ OH (Inset: Tauc plot for the bandgap estimation).	115
Figure 4.23	PL spectra (excited at 325 nm) of the colloidal ZnSiQD suspension in acetone synthesised (a) without and (b) with NH ₄ OH (20 μ L). ..	116
Figure 4.24	PL spectra (excited at 365 nm) of the colloidal ZnOSi QDs synthesised with NH ₄ OH of (a) 15 μ L, (b) 20 μ L, and (c) 25 μ L. ..	118
Figure 4.25	(a) Excitation spectra of the source at excitation peak of (1) 365 nm, (2) 390 nm, and (3) 425 nm. (b) PL spectra of the colloidal ZnSiQD suspension in containing 25 μ L of NH ₄ OH excited at the wavelengths of (1) 365 nm, (2) 390 nm, and (3) 425 nm.	119

Figure 4.26	UV–Vis absorbance of the colloidal ZnOSi QDs suspension in acetone synthesised with NH ₄ OH of (a) 15 μL (b), 20 μL, and (c) 25 μL.....	120
Figure 4.27	The schematic diagram for the mechanism of NH ₄ OH influence on the ZnO shell.....	122
Figure 4.28	FESEM image of the film deposited on ITO glass substrate and (b) and (c) the corresponding EDX elemental traces.....	123
Figure 4.29	XRD patterns of TiO ₂ NPs deposited on ITO substrate after annealing at temperatures (a) 200, (b) 300, and (c) 400 °C.....	123
Figure 4.30	EFTEM morphology of the TiO ₂ NPs annealed at (a) 200, (b) 300, and (c) 400 °C.....	124
Figure 4.31	XRD patterns of the TiO ₂ NPs deposited on Si substrate after annealing at temperatures (a) 500, (b) 550, (c) 600 and (c) 650 °C.....	125
Figure 4.32	Annealing temperature-dependent variation in the crystallite size and FWHM of the studied films.....	126
Figure 4.33	The optical absorbance of the TiO ₂ NPs annealed at different temperatures.....	127
Figure 4.34	Optical absorbance of TiO ₂ NPs against annealing temperature.....	128
Figure 4.35	Effect of annealing temperature on the E _g	128
Figure 4.36	FESEM images top-view together with corresponding particles size distribution and cross-section view (inset) of TiO ₂ NPs deposited on Si substrate and annealed at temperatures (a) 500, (b) 550, (c) 600 and (d) 650 °C.....	129
Figure 4.37	Diffuse reflectance spectrum of c-Si substrate with TiO ₂ NPs annealed at 600 °C.....	130
Figure 5.1	FESEM image (top view) combined with the reflection of PSi at various etching times of (a) 30 s, (b) 60 s, (c) 90 s, and (d) 120s...	133
Figure 5.2	FESEM image (cross-section) combined with the reflection of PSi at various etching times of (a) 30 s, (b) 60 s, (c) 90 s, and (d) 120 s. (e) Etching time versus bandgap of PSi.....	135

Figure 5.3	AFM morphology of PSi etched at (a) 30 s, (b) 60 s, (c) 90 s, (d) 120 s.	137
Figure 5.4	Etching time versus RMS and average R of PSi.....	138
Figure 5.5	(a) PL spectra of PSi etched at numerous etching times, (b) etching time versus RMS roughness and peak emission wavelength.....	139
Figure 5.6	(a) Current density versus voltage at various etching times for Al/c-Si/PSi/Ag, (b) carriers concentration of PSi etched at different etching times.	141
Figure 5.7	Architectures of the proposed solar cells obtained using TiO ₂ NPs -enclosed thin film as ETL.....	143
Figure 5.8	Photovoltaic performance of the proposed cells fabricated without and with TiO ₂ NPs (a) I-V characteristics (b) PCE and FF, (c) J _{SC} and V _{OC}	144
Figure 5.9	Performance of cells fabricated with annealed (500 °C) TiO ₂ NPs film (a) I-V characteristics, cell configuration together with PCE, FF, J _{SC} , and V _{OC} , and (b) showing the mechanism of electrons tunnelling, carriers' generation across the energy bandgap.	147
Figure 5.10	Architectures of the GBQDSCs (a ₁) ZnOSi QDs size of 7.4 nm, (b ₁) ZnOSi QDs size of 2.7 nm and (c ₁) ZnOSi QDs size of 2.1 nm. (a ₂) Reflection spectra of SL-ZnOSi QDs and (b ₂) AFM image of p-c-Si/PSi/ZnOSi QDs (7.4 nm)/ TiO ₂ NPs (RMS roughness of 0.859 nm).	150
Figure 5.11	Performance comparison of the cells made of Al/p-c-Si/PSi/Ag, Al/p-c-Si/PSi/ TiO ₂ NPs/Ag, Al/p-c-Si/PSi/ZnOSi QDs/TiO ₂ NPs/Ag (ZnOSi QDs mean size of 7.4 nm), Al/p-c-Si/PSi/ZnOSi QDs/TiO ₂ NPs/Ag (QDs mean size of 2.7 nm) and Al/p-c-Si/PSi/ZnOSi QDs/TiO ₂ NPs/Ag (QDs mean size of 2.1 nm).....	151
Figure 5.12	Architectures of the solar cells obtained with PSi, TiO ₂ NPs (a ₁), (b ₁), and (c ₁) DL-ZnOSi QDs; (d ₁) and (e ₁) TL-ZnOSi QDs. FESEM image (a ₂) cross-section view of TL-ZnOSi QDs cell and (b ₂) top view of PSi and pores size distribution (histogram) with	

Gaussian fit (blue curve). Performance of PV fabricated with (a₃) DL-ZnOSi QDs and (b₃) TL-ZnOSi QDs. Reflection spectra of the solar cell made with (a₄) DL-ZnOSi QDs and (b₄) TL-ZnOSi QDs.

..... 156

Figure 5.13 (a₁) Energy band diagram of the solar cell Al/p-c-Si/PSi/ZnOSi QDs (2.3 eV)/ZnOSi QDs (2.5 eV)/ZnOSi QDs (3.3 eV)/TiO₂ NPs/Ag. (a₂) showing the mechanism of inserted Zn⁺² into Si QDs, (a₃) I-V characteristics and (a₄) Energy band diagram of the structure of Al/p-c-Si/PSi/ZnOSi QDs (3.3 eV)/ZnOSi QDs (2.5 eV)/ZnOSi QDs (2.3 eV)/TiO₂ NPs/Ag..... 159

LIST OF SYMBOLS

σ	Electrical conductivity
Ω	Electrical resistance
K	Boltzmann's constant
h	Plank's constant
\hbar	Modified Plank's constant
m_e^*	Electron effective mass
m_h^*	Hole effective mass
ν	Frequency

LIST OF ABBREVIATIONS

PL	Photoluminescence
PSi	Porous silicon
Zn	Zinc
HF	Hydrofluoric acid
C ₂ H ₅ OH	Ethanol
QDs	Quantum dots
Si QDs	Silicon quantum dots
ZnOSi QDs	Silicon quantum dots integrated with zinc.
ZnO	Zinc oxide
NH ₄ OH	Ammonium hydroxide
TiO ₂	Titanium dioxide
nm	Nanometer
eV	Electron volt
XRD	X-ray diffraction
°C	Celsius degree
GBG SCs	Graded bandgap solar cells
GBQD SCs	Graded bandgap quantum dots solar cells
mA/cm ²	Milliamperes per square centimetre
TiO ₂ NPs	Titanium dioxide nanoparticles
PV	Photovoltaic
QDSSCs	Quantum dot sensitized solar cells
MEG	Multiexciton generation
AM	Air mass
PCE	Power conversion efficiency
E _g	Energy bandgap
e	Electron
h	Hole
GaAs	Gallium arsenide
Al	Aluminium
R, G	Recombination and generation
KE	Kinetic energy

IR	Infrared
E_v	Highest of the valence band
E_c	Lowest of the conduction band
PbS	Lead Sulfide
CdSeTe	Cadmium Selenide Telluride
ZnS	Zinc Sulfide
CdS	Cadmium Sulfide
InAs	Indium Arsenide
InGaAs	Indium Gallium Arsenide
R	Reflection
p-c-Si or p-Si	p-type crystalline Silicon
n-c-Si or n-Si	n-type crystalline Silicon
Ag	Silver
Au	Gold
n_i	Intrinsic carrier concentration
N_c	Effective density of states at the conduction band
N_v	Effective density of states at the valence bands
T	Temperature
RT	Room temperature
J	Joule
E_F	Fermi level
As	Arsenic
P	Phosphorus
Sb	Antimony
B	Boron
CB	Conduction band
VB	Valence band
C	Carbon
Ge	Germanium
m	Mass
v	Velocity
LEDs	Light-emitting diodes
PSi-O	Porous silicon oxide
H^+	Hydrogen ions

Pt	Platinum
Cu	Copper
F	Fluoride
m^2/cm^3	Meter square per centimetre cube
Δx	Change in distance
Δp	Change in momentum
Fe	Iron
Mn	Manganese
V	Vanadium
Ti	Titanium
Co	Cobalt
Ni	Nickel
SPR	Surface plasmon resonance
Rsh	Shunt resistance
Φ_b	Barrier height
La	Lanthanum
RF	Radio Frequency
DC	Direct current
ALD	Atomic layer deposition
VO^+ , VO^{++}	Single and double charge vacancy
EMA	Effective mass approximation
n_1, n_2, n_3	Quantum numbers
PEDOT:PSS	Poly (3, 4-methylenedioxy-thiophene)/poly (styrenesulfonate)
PTB7	Poly[[4,8-bis[(2-ethylhexyl)oxy]benzo[1,2-b:4,5-b']dithiophene-2,6-diyl][3-fluoro-2-[(2-ethylhexyl)carbonyl]thieno[3,4-b]thiophenediyl]]
HOMO	Highest occupied molecular orbital
LOMO	Lowest unoccupied molecular orbital
C_{60}	Carbon nanostructure
SWCNTs	Single-walled carbon nanotubes
ITO	Indium tin oxide
C_3H_6O	Acetone
PVP	Polyvinylpyrrolidone
UV-Vis	Ultraviolet-visible
FTIR	Fourier transform infrared

SEM	Scanning electron microscopy
FESEM	Field-emission scanning electron microscope
EDS	Dispersive X-Ray Spectrometer
STEM	Scanning transmission electron microscopy
EBSD	Electron backscatter diffraction
HRTEM	High-resolution transmission electron microscope
EFTEM	Energy-filtered transmission electron microscopy
CCD	Charge-coupled device
AFM	Atomic force microscopy
d	Distance between the planes
FWHM	Full-width half maximum
XPS	X-ray photoelectron spectroscopy
ESCA	Electron spectroscopy for chemical analysis
$h\nu$	Photon energy
BE	Binding energy
I_0	Dark saturation current
NREL	National renewable energy laboratory
EQE	External quantum efficiency
HJCS	Heterojunction solar cells
ETL	Electron transport layer
HTL	Hole transport layer
E_e	The practical gap energy
ER	Etching rate
W	Watt
ρ	Density
S	Area
m_1	Mass of the sample before etching.
m_2	Mass of the sample after etching
m_3	Mass of the sample after removing the PSi layer
d	The thickness of the PSi
MIS-SC	Metal insulator semiconductor solar cells
SC	Solar cells
QCE	Quantum confinement effect
QY	Quantum yield

**BINTIK KUANTUM SILIKON TERBITAN SILIKON BERLIANG
DENGAN ZINK OKSIDA TERGABUNG UNTUK APLIKASI
FOTOVOLTAN**

ABSTRAK

Beberapa logam peralihan telah digunakan bagi meningkatkan sifat optik semikonduktor. Zink (Zn) telah dimasukkan ke dalam silikon berliang (PSi) dan bintik kuantum silikon (Si QDs) untuk meningkatkan sifat optik dengan mengurangkan kadar pengoksidaan. Koloid Si QDs yang disepadukan dengan Zn oksida (ZnOSi QDs) diperoleh daripada PSi yang dipunar secara elektrokimia dengan tambahan Zn dan diikuti dengan sonikasi, proses tersebut dipanggil sebagai proses atas-bawah. Spektrum pancaran ZnOSi QDs yang dikaji adalah terutamanya, berkait dengan kesan pengurangan kuantum dan lapisan permukaan zink oksida (ZnO) pada Si QDs yang meminimumkan pengoksidaan Si. Penggabungan proses atas-bawah dan bawah-atas membawa kepada penghasilan pelbagai jurang tenaga ZnOSi QDs yang bergantung kepada faktor saiz zarah; maka kekurangan yang dihadapi Si QDs seperti cabaran untuk menghasilkan zarah bersaiz seragam dan Si QDs teroksida selepas proses elektrokimia akibat pendedahan ambien, telah diatasi. Kaedah bawah-atas telah digunakan bagi penghasilan semula ZnOSi QDs yang mempunyai pelbagai saiz dan bentuk yang seragam melalui pertumbuhan semula Si QDs yang dilitupi oleh ZnO. Filem nipis yang mengandungi nanozarah titanium dioksida (TiO₂ NPs) telah disediakan daripada titanium hidroksida (Ti(OH)₄). TiO₂ NPs berbentuk sfera dengan purata saiz antara julat 3.2 nm hingga 33.94 nm telah digunakan bagi meningkatkan kadar pengekstrakan cas yang terhasil melalui penjanaan foto. Sel suria bintik kuantum jurang jalur bergred (GBQDSCs) telah difabrikasi berdasarkan bahan bukan toksik

seperti Si QDs dan TiO₂ NPs. Lapisan ZnOSi QDs dengan pelbagai saiz telah dimasukkan antara PSi dan TiO₂ NPs untuk mencapai GBQDSCs. Hasilnya, sel yang dicadangkan telah mencapai kecekapan sebanyak 4.9%. Tambahan pula, ia menunjukkan bahawa prestasi sel boleh dipertingkatkan dengan mengoptimumkan penjajaran tahap tenaga dalam lapisan PSi, ZnOSi QDs, dan TiO₂ NPs.

**SILICON QUANTUM DOTS DERIVED FROM ZINC OXIDE
INCORPORATED POROUS SILICON FOR PHOTOVOLTAIC
APPLICATIONS**

ABSTRACT

The transition metals were used to enhance the optical properties of the semiconductor. Zinc (Zn) was inserted in porous silicon (PSi) and silicon quantum dots (Si QDs) to improve the optical properties by reducing oxidation. The colloidal Si QDs integrated with Zn oxide (ZnOSi QDs) were obtained from the electrochemically etched PSi with Zn inclusion followed by the sonication, that process called the top-down process. The emission spectra of the studied ZnOSi QDs were mainly ascribed to the effects of quantum confinement and zinc oxide (ZnO) surface layer on the Si QDs that minimized the Si oxidation. The combining top-down and bottom-up processes led to producing ZnOSi QDs of various bandgaps depending on the particles size; hence drawbacks encounter Si QDs such as the challenge to produce particles of uniform size and Si QDs oxidized after the electrochemical process due to ambient exposure, were exceeded. The bottom-up method was used to reproduce these ZnOSi QDs with various uniform sizes and shapes by regrowth of the Si QDs, which ZnO covered. Thin films containing titanium dioxide nanoparticles (TiO₂ NPs) were prepared from titanium hydroxide (Ti(OH)₄). Spherical TiO₂ NPs of average size in the range of 3.2 nm to 33.94 nm were utilised to improve the extraction of photo-generated charges. The graded bandgap quantum dots solar cells (GBQDSCs) were fabricated based on non-toxic materials such as Si QDs and TiO₂ NPs. ZnOSi QDs layers of various sizes were inserted between the PSi and TiO₂ NPs to achieve GBQDSCs. As a result, the proposed cell attained an efficiency of 4.9%. Furthermore,

it was shown that the cell performance could be enhanced by optimizing the energy levels alignment in the P-Si, ZnO/Si QDs, and TiO₂ NPs layers.

CHAPTER 1

INTRODUCTION

1.1 Overview

Quantum dot sensitized solar cells (QDSSCs) are considered one of the third generation's innovative solar cells due to the excellent optoelectronic of QDs light absorber properties, such as significant absorption coefficient, flexible light-harvesting capability, high stability and low-cost availability. In comparison, the theoretical limit of QDSSCs power conversion efficiency (PCE) can be beyond the level of Shockley–Queisser (33.7%) due to the multiexciton generation (MEG) [1,2]. Shockley-Queisser limit is the maximum PCE for the p-n solar cell at 1.5 air mass (AM), and the bandgap is 1.34 eV, where the loss only is radiative recombination. In reality, the maximum PCE does not reach to Shockley-Queisser limit due to the high amount of light reflected from the surface [3,4]. Figure 1.1 shows the pathways of the energy loss through the homogeneous junction. The two most important causes of power loss in single-band photovoltaic devices are photons with less energy than the bandgap and photons above the bandgap.

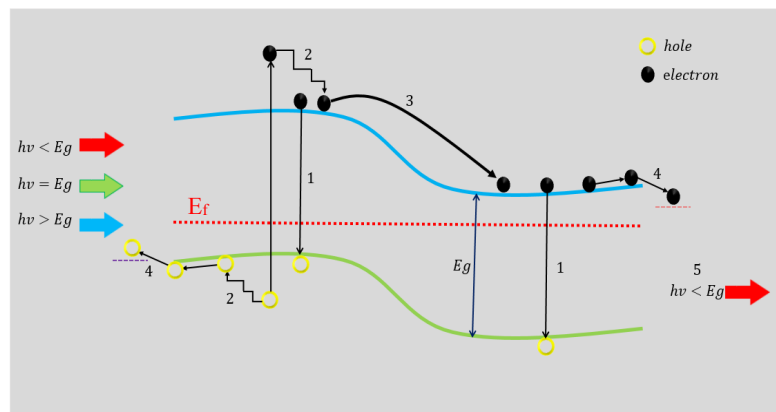


Figure 1.1 An energy band diagram showing the major energy loss pathways: (1) recombination loss; (2,3, and 4) thermalization loss ; (5) photons with insufficient energy cause non-absorption.

Therefore, three solutions were proposed to solve those problems [1]: (a) varying the value of bandgaps through the cell to absorb a broad range of the solar spectrum, (b) extraction of the carriers before thermalization and (c) MEG per high energy photon.

1.2 Background of Graded Bandgap Solar Cells

When it comes to solar cells, the essential notion behind GBGSCs is the ability of effective photon harvesting across the ultraviolet (UV), visible (Vis), and infrared (IR) wavelength ranges. This notion has been proven in the literature across the spectrum of solar cell technologies, including organic, inorganic, and hybrid [5,6]. Furthermore, it is possible to achieve a graded bandgap by grading the absorber layer so that the bandgap differs along with its whole thickness. An alternative method of creating a GBGSCs is to stack layers of semiconductor materials on top of one another, with the layers being structured so that the bandgap drops progressively.

Tauc published the first theoretical description of the functionality of the GBGSCs arrangement in 1957, which was the year before the GBGSCs were invented. In his work, he has demonstrated that GBGSCs can achieve higher conversion efficiency than the more well-known p-n junction cells, which has sparked attention in the photovoltaic research community. Based on the photo-generated current, it has been theoretically demonstrated that GBGSCs designs can achieve conversion efficiencies of 38%, which is significantly higher than the 23% achieved by single p-n junction solar cells. Regarding the theoretical concept, the first sets of GBGSCs were built and published in the 1970s by gradually doping p-type gallium arsenide (GaAs) with aluminium (Al), and the results were published [7]. The published work exhibited a single-sided p-type grading of a p-Ga_{1-x}Al_xAs/n-GaAs solar cell with a single-sided

p-type grading. Dharmadasa et al. (2002) [8] devised and published the first model of whole solar cell device bandgap grading in 2002, the first model of its kind. As seen in Figure 1.2, the GBGSCs described by Dharmadasa et al. (2005) [9] can be made more efficient by including either an n-type or a p-type wide bandgap front layer with a gradual drop in bandgap towards the p-type or n-type back layer, respectively. Because of the higher theoretical barrier height that can be achieved with this method, the devices constructed with it are more favourable [6]. The following are some of the advantages of GBGSCs:

1. The prospect of collecting photons from across the solar radiation (in the ultraviolet, visible, and infrared ranges) is explored.
2. The decreased thermalization of "hot carriers" results from shared photon absorption across different solar cell sections.
3. The occurrence of an electric field (or depletion width) that extends essentially throughout the whole thickness of the solar cell results in an improvement in e-h pair capture and, consequently, reduces recombination (R).
4. The integration of impurity PV impacts ionization into GBGSCs architectures to lower recombination (R)/generation (G) and boost photo-generated current density.

The e-h pairs created by the absorption of high-energy photons, as illustrated in Figure 1.2, are efficiently split by the strong built-in electric field throughout the solar cells according to the fundamental basic concepts of solar cells. The electron is forced to move towards the back contact by the strong built-in electric field caused by the steep gradient created by the device structure. As seen in Figure 1.2, an electron travelling at high kinetic energy (KE) can transmit its momentum to atoms near the back end of the GBGSCs structure and break inter-atomic bonds, resulting in other e-h pairs. Band-to-band effect ionization is the name for this phenomenon.

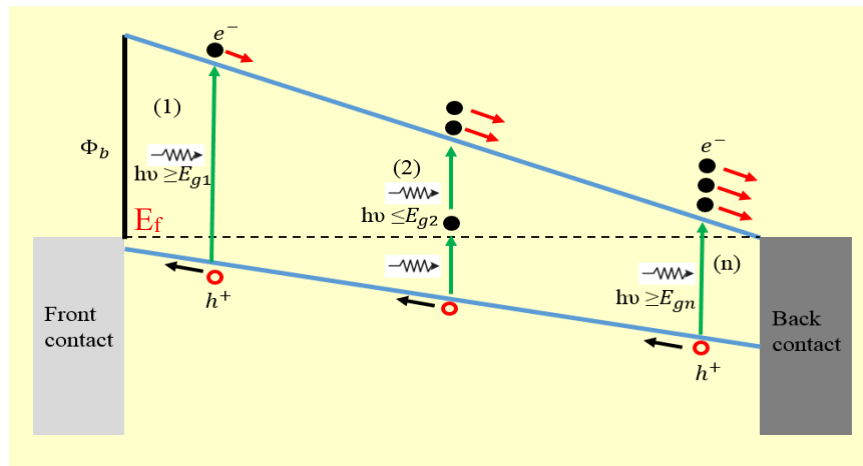


Figure 1.2 Diagram of GBGSCs [5].

It is also probable that IR is linked to e-h pair formation, perhaps directly through the excitation of an electron from the highest of the valence band (E_v) to the lowest of the conduction band (E_c); or often by the promotion of electrons to defect states inside the forbidden gap, as Figure 1.2. Recombination of the e-h pairs may be prevented in the GBG device because of the direct transmission of the electron's paired hole due to the strong electric field in the device [6]. As a result, the electron becomes trapped in the defect level until it is promoted to the conduction band by additional absorption of an infrared photon. In addition, there is the possibility of having both the impact ionization and the impurity photovoltaic (PV) effect mechanisms operate simultaneously. This is accomplished by transmitting momentum from a high KE electron accelerating to the rear end of the GBGSCs device to promote the trapped electron in the defect level during the impurity PV effect, known as electron promotion. The avalanche effect occurs due to both impact ionization and impurity PV effect occurring throughout this phase.

1.3 Problem Statement

The increased earth temperature and weather variation are the main environmental issues in the world in the last few years, which are increased with the increasing use of conventional energy sources such as oil, gas, and charcoal. Therefore, to reduce these problems, the traditional energy sources should be mixed with clean energy sources, such as wind, water, sea waves, solar energy, etc. The sun is considered the primary source of power on the earth, and it is a renewable and environmentally friendly energy [10]. Therefore, various solar cells were fabricated to generate electric energy, such as crystalline silicon (c-Si) cells, thin-film cells, dye-sensitized solar cells (DSSCs), organic solar cells (OSCs), perovskites photovoltaics (PVs), kesterite PVs, and quantum dots sensitized solar cells (QDSSCs). Theoretically, the efficiency of QDSSCs was more than 66% due to MEG extracted before recombination; this has attracted many researchers to study this type of solar cell [10]. However, in reality, the maximum efficiency of QDSSCs was around 13% to 16%. Furthermore, the size of a QDs determines its bandgap; hence the real benefit of a QDs cell is that its bandgap can be accurately adjusted by adjusting its size [11].

Over the last years, QDSSCs established on QDs such as lead(II) sulfide (PbS), cadmium selenium telluride (CdSeTe), cadmium selenium (CdSe), zinc sulfide (ZnS), cadmium sulfide (CdS), indium arsenide (InAs), indium gallium arsenide (InGaAs), etc., have enhanced dramatically. These solar cells are made of toxic metals, including lead (Pb) and cadmium (Cd), which are strictly controlled in electronic consumer goods in various countries [12,13], or rare metals such as In, which increase the manufacturing cost [14]. Thereby, it is crucial to produce non-toxic and low-cost quantity QDs such as Si, ZnO, TiO₂, and graphene (Gr).

Several drawbacks encountered Si QDs created by the top-down process (electrochemical etching and laser ablation), such as it is challenging to produce particles of uniform size and shape in this way. However, the particles size is in the range of micrometer to nanometer [15]. Therefore, it is necessary to develop a physical or chemical method to control the size and shape of the particles. Furthermore, Si QDs oxidized after the electrochemical process due to ambient exposure, creating shallow and deep-level defects within the Si bandgap. These defects act as traps levels or recombination centres for photo-generated carriers [16]. Therefore, to reduce the native oxide of Si QDs, the particles must be coated before exposure to ambient.

Low absorbance (owing to the inability to cover the long-wavelength area of the sun spectrum) [17], and high reflection ($> 30\%$) [18,19]; lead to limiting the performance of many types of solar cells by reducing the current density, resulting from a decrease in the extraction of the number of photo-generated charges. This reduction was increased in solar cells containing QDs if the energy levels did not align, boosting the thermalization loss [20]. The dynamics of interfacial electron transfer are critical to QDSSCs and DSSCs. Improvements in device performance depend on optimizing these interfacial dynamics and, particularly, the development of film structures that minimize interfacial recombination dynamics relative to charge transport through the film [21]. It is well known that the size and shape of Si QDs nanostructures significantly impact their characteristics. The efficiency of their applications, such as light-emitting diodes (LEDs), photodetectors and solar cells, is strongly reliant on their size and shape, and reasonable control during synthesis is required to obtain a homogeneous shape and the desired size for these particles.

The energy level alignment between the conduction band of Si QDs and the conduction band for different layers leads to allowing or preventing the extraction of electrons. For example, the conduction band energy for bulk Si and TiO₂ is - 4.0 eV and - 4.02 eV, respectively. The band energy for bulk Si and TiO₂ is - 5.1 eV and - 7.25 eV, respectively. Therefore, the conduction band and the valence band energy for nanoparticles will be expanded and split to reduce the particle size. Consequently, the conduction band energy and valence band energy for Si QDs become larger than bulk Si. As a result, increasing the injected electrons were transferred swiftly from the interface of the layers and reducing recombination losses by increasing the relaxation time. Hence, the extraction of electrons and holes is growing, thereby enhancing solar cell performance. In addition, the relaxation time for the nanoparticle is larger than the bulk state because of the increase in the distance between the energy levels, thereby leading to a reduced recombination process and increasing the extraction probability of charge carriers [22].

In short, this research aims to synthesise non-toxic QDs such as Si and TiO₂ with various bandgaps. These nanoparticles are used to fabricate graded bandgap solar cells depending on the particle size and bandgap value. Therefore, this research did not aim to develop high-efficiency GBQDSCs, but rather to synthesise and characterize non-toxic and low-cost quantum dots, which will be used in solar cells. In addition, to understand better the mechanisms that control the performance of the solar cells based on Si QDs, PSi, and TiO₂ NPs.

1.4 Objectives

- 1- To enhance the optical properties of the PSi and Si QDs by reducing the oxidation of the PSi by Zn.

- 2- To produce ZnOSi QDs of various bandgaps depending on the particles size by combining top-down and bottom-up processes.
- 3- To improve the extraction of photo-generated charges by utilising TiO₂ NPs.
- 4- To fabricate GBQDSCs structures based on non-toxic materials such as Si QDs and TiO₂ and characterize

1.5 Hypothesis

- The reducing particle size increases bandgap energy, which is a shift in the edge of the conduction and valance band energy. Suppose the conductive energy levels between the other layers align. The electrons will inject from the higher level to the lower level, which improves the photo-generated current.
- The optical and electrical properties for ZnOSi QDs and TiO₂ NPs depend on the size, surface chemical bond, and defects. If the particle size is modified to absorb a broad range for the solar spectrum, that leads to enhancement of the PCE of the solar cell by increasing the absorption range.

1.6 Scope of Study

Solar cells with a graded bandgap will be fabricated in the present work. ZnOSi QDs can absorb a broad region of the solar spectrum that depends on the bandgap energy. Si QDs absorb light in the short wavelength region, and the recombination process emits light in the visible region. Suppose Si QDs are used as an active layer

with several sub-layers (~1 nm, ~2 nm, ~7 nm) that layers have a unique size and unique bandgap. Each layer will absorb a part of the solar spectrum, small particles absorb the shortest wavelength, and the largest particle size absorbs the longer wavelength.

Firstly, the Si QDs were synthesised by the top-down method with optimum conditions to achieve the smallest size of the Si QDs. Next, these QDs were utilised to produce various Si QDs sizes through the bottom-up method.

1.7 The Originality of the Study

The originality of this study is summarised by:

- Preparing silicon quantum dots from zinc oxide incorporated porous silicon
- Regrowing of ZnOSi QDs to achieve various sizes
- fabricating graded bandgap solar cells with ZnOSi QDs, PSi and TiO₂ NPs.

1.8 Thesis Outline

The thesis is divided into six chapters, beginning with the study introduction about solar cells and GBSCs, problem statement, aims, hypothesis, the scope of the study, the originality, and thesis outline.

Chapter two offers a history of the material classification, which consist of dopants-based classification, band symmetry-based classification, porous silicon, which consists of the mechanism of electrochemical, electrochemical etching, PL of the PSi, enhancement of the PSi properties by organic and inorganic materials, Si QDs

properties which consist of Si QDs nanostructures with quantum confinement, TiO₂ NPs properties, the solar cell containing a quantum dot and P-Si which consist of solar cell device junctions and interfaces, types of the solar cells and principle work, utilising P-Si in the solar cell.

Chapter three describes the synthesis of Si QDs particles, TiO₂ NPs, solar cell fabrication, devices manufacture, and characterizations.

Chapter four presents results and discussions of ZnO/Si QDs, and TiO₂ NPs, while chapter five discusses the optical and electrical characterization of the GBQDSCs. Chapter six consists of the conclusions and future works.

CHAPTER 2

LITERATURE REVIEW

This chapter is divided into nine sections. It is concerned with a literature review and the scientific background of material classification, semiconductor classification, the properties of PSi, Si QDs, and TiO₂ NPs, and the types of solar cells. Different types of junctions and interfaces in solar cells will be discussed.

2.1 Material Classification

All materials are classified as conductors, semiconductors, or insulators based on their electrical characteristics. Semiconductors are fascinating because they have features between conductors and insulators. For example, they have less conductivity than conductors but a higher conductivity than insulators [23]. Table 2.1 summarises the conductor, insulator, and semiconductor [24].

Table 2.1 The list of essential qualities of various solid-state materials [24].

Parameter	Electrical conductors	Semiconductors	Electrical insulators
Electrical conductivity σ ($\Omega \text{ cm}$) ⁻¹	$\sim 10^6 - 10^0$	$\sim 10^0 - 10^{-8}$	$\sim 10^{-8} - 10^{-20}$
Bandgap E_g (eV)	≤ 0.3	$\sim 0.3 - 4.0$	> 4.0

Certain semiconductors have revolutionized human civilization and enabled incredible technical progress. The term "semiconductor" can be used to describe two types of semiconductors: intrinsic and extrinsic semiconductors. There are no impurities in intrinsic semiconductors, indicating clean or undoped, that allow them to have an equal number of positive (holes) and negative (electrons) charges [25]. Thermal excitation forms a pair of electrons and holes in an intrinsic semiconductor.

The relation between their intrinsic carrier concentration (n_i) can be expressed by the Equation 2.1 [26]

$$n_i = \sqrt{N_v N_c} e^{-\frac{E_g}{2kT}} \quad (2.1)$$

The effective density of states at the conduction and valence bands are denoted by N_c and N_v , respectively. E_g is the energy gap (between the bottom conduction band (E_c) and the top of the valence band (E_v)) because there are no electrons in this band; it is also known as the forbidden band. k is Boltzmann's constant of 1.38×10^{-23} J/K, and T is the temperature in Kelvin.

2.2 Dopants-Based Classification

The Fermi level is the maximum energy level can the electron reach at absolute zero temperature. The Fermi level's value indicates the material type. The Fermi level is located precisely in the middle of the energy band because an intrinsic semiconductor does not have impurities. Figure 2.1 depicts an energy band diagram of an inherent [27]. Extrinsic semiconductors are not pure and are doped. The extrinsic semiconductor is classified into two types based on the numerical value of the charge concentration. They are n-type and p-type semiconductors. An n-type semiconductor is one in which the concentration of electrons is greater than that of holes. In general, n-type semiconductors are made by doping a pure semiconductor with a material that has five valence electrons in the outer shell [28]; Arsenic (As), phosphorus (P), and antimony (Sb) are examples of these types of materials in the periodic table, assuming Si is the host atom. These materials are commonly referred to as donors because they give away their electrons when combined with an intrinsic semiconductor. Figure 2.2 depicts the electronic structure of extrinsic semiconductors.

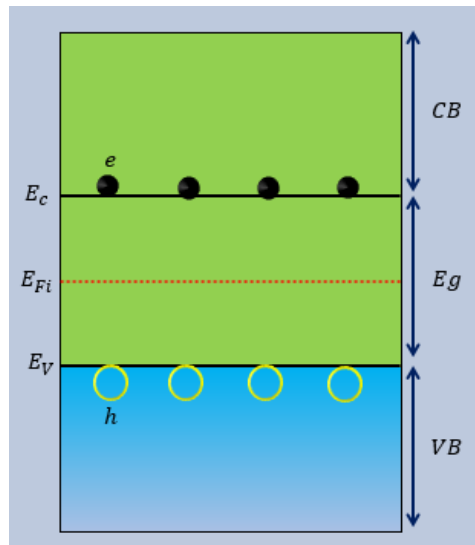


Figure 2.1 An intrinsic semiconductor's energy band diagram.

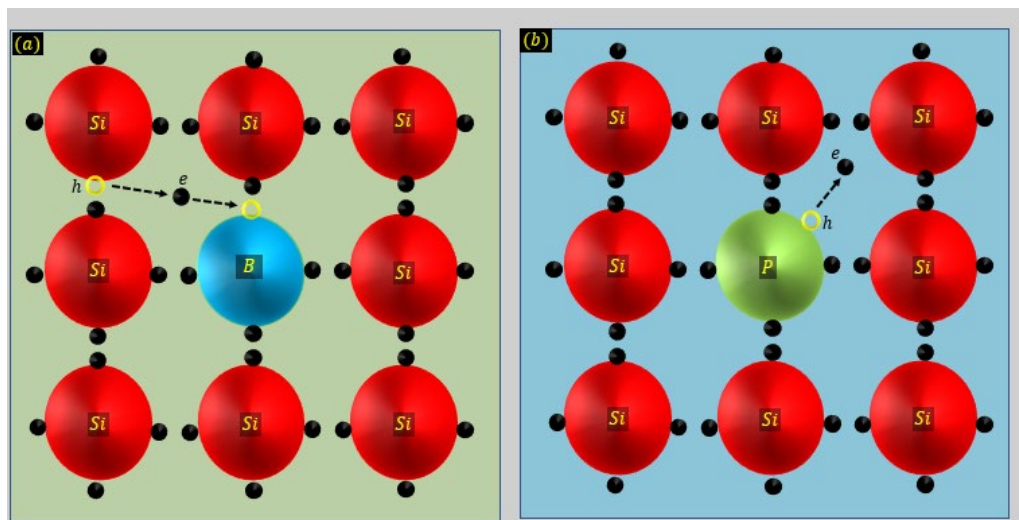


Figure 2.2 Electronic structures of Si-doped with (a) boron and (b) phosphorus.

P-type semiconductors have a higher density of holes than electrons. P-type semiconductors are made by doping them with materials that contain three valence electrons in their outer shell, such as boron (B), aluminium (Al), gallium (Ga), and indium (In). These materials are called acceptors because they remove electrons from the Si, resulting in a vacancy in the Si atom. These vacancies are holes. Figure 2.3 depicts the energy band diagram of extrinsic semiconductors.

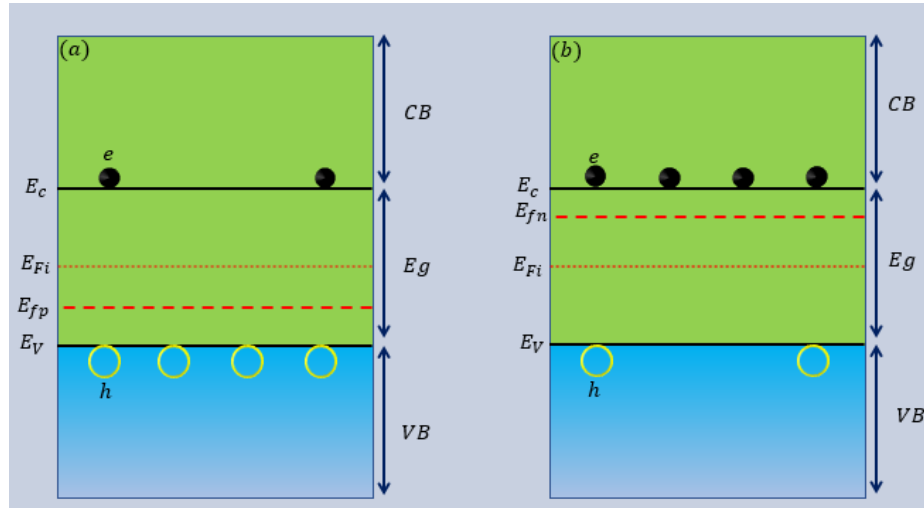


Figure 2.3 Energy band diagram of (a) p-type and (b) n-type semiconductor.

Depending on their chemical composition, semiconductor materials can be summarised as elemental, binary, ternary, and quaternary semiconductors; Table 2.2 summarises the common semiconductors used in PV devices [24].

Table 2.2 Lists of semiconductor elements and compounds used in PV devices are provided below [24].

Semiconductor category	Example
Single-atom	C, Si, Ge
Binary	III–V: AlN, AlP, AlAs, AlSb, GaN, GaP, GaAs, GaSb, InN, InP, InAs, InSb. II–VI: ZnS, ZnSe, ZnTe, ZnO, CdS, CdSe, CdTe, CdO
Ternary	CuInSe ₂ (CIS), Cd _x Mn _(1-x) Te (CMT), Cd _x Hg _(1-x) Te, Al _x Ga _(1-x) As
Quaternary	CuInGaSe ₂ (CIGS), AgInGaSSe ₂ , Cu ₂ ZnSnSSe ₄ (CZTS)

2.3 Energy Band Origination

There are three energy levels in semiconductor crystals: the valence band energy level, the Fermi level energy, and the conduction band energy level. When two

atoms are brought into proximity, their atomic orbitals combine to form molecular orbitals. The equilibrium states of the energy bands are disturbed due to this process, following Pauli's exclusion principle [29]. As a result, a band of energies is created that is continuous. Most electrons are in the lowest energy band, known as the valence band (VB). The conduction band (CB), the highest energy band, contains very few electrons [28].

2.4 Band Symmetry-Based Classification

The matching of electron momentum (p) of the minimal energy difference between the E_c and E_v can classify semiconductors. The architectural patterns of energy-momentum (E-k) displays for direct and indirect bandgap semiconductors are shown in Figures 2.4(a, b), respectively.

$F = m^*a$ (m^* is the effective mass of the electron or hole concerned in the transition, a is the acceleration, and v is the velocity) is the traditional formula for the force on every charge carrier. The kinetic energy (KE) of a charge carrier, as described in Equation 2.2 ;

$$KE = \frac{p^2}{2m^*} = \frac{m^*v^2}{2} = \frac{\hbar k^2}{2m^*} \quad (2.2)$$

$p = m^*v$ or $p = \hbar k$, where \hbar is the modified Plank's constant, denoted by $\frac{h}{2\pi}$, and k is the wave vector, represented by $\frac{2\pi}{\lambda}$.

Both E_c and the E_v occur at the exact value of the wave vector for direct bandgap semiconductors. That means if an electron at E_v has enough energy, it can migrate to the E_c without changing its wave vector [30,31], as shown in Figure 2.4(a). On the other hand, indirect bandgap semiconductor materials exhibit the E_c and E_v at various wave vectors, as illustrated in Figure 2.4(b). In an indirect bandgap semiconductor, phonons that hold considerable momentum compensate for the

variance in momentum in an electron energy transition [24,30]. This involvement of phonons is required for momentum saving on affecting electron transfer. A direct bandgap material is favoured for optical operations such as the PV effect or light emission due to the higher possibility of an electron transitioning from the valence band to the conduction band or vice versa [24].

Figure 2.4 depicts the E-K diagram. The photons must have minimum energy equal to the bandgap to excite the electrons from the valence band to the conduction band, thus free to move within the lattice. Carrier generation and carrier recombination are defined as the incident of photon absorption exciting an electron and then returning that excited electron to fill the vacancy; respectively, they are two terms that are frequently used in the PV field. The bandgap energy is critical because it is connected to the absorbed and emitted photons [31].

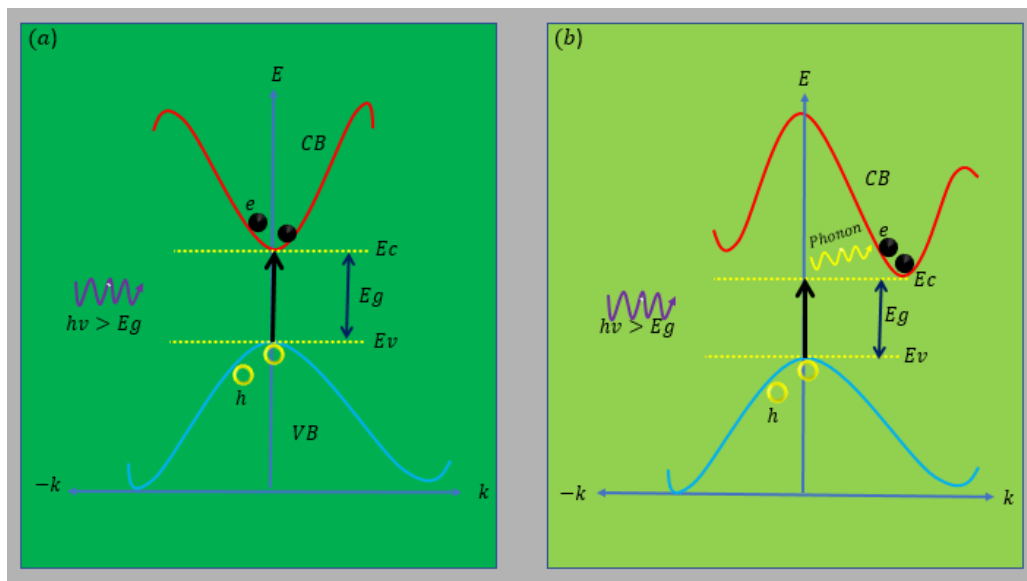


Figure 2.4 (a) Direct and (b) indirect bandgap semiconductor.

2.5 Porous Silicon

2.5.1 Overview

Recent research on PSi has opened new avenues for a broad range of applications such as advanced optoelectronic devices, biological sensors, and solar energy conversion [32]. The material, in its micro-, and nano- phases, is a promising candidate for diverse photonic applications. PSi as an anti-reflection layer is used in integrated optoelectronic devices such as LEDs, and biosensors [33,34] because they emit PL efficiently at room temperature and are compatible with normal Si manufacturing [35].

Over the years, numerous methods have been introduced to prepare high-quality doped and undoped PSi with controlled porosity, structure, and morphology to fulfill the increasing industrial demand for functional Si devices. For instance, etching methods, focused ion beam lithography, electron beam lithography, and rapid thermal annealing. Etching techniques include stain etching, photoetching, metal-assisted etching, vapour etching, reactive-ion etching, electrochemical etching, laser ablation, spark erosion, laser-induced plasma erosion Si deposition by high-density plasma, reduction of porous silica, laser-induced silane decomposition, and wet chemical etching of Si [36]. The formation of PSi is generally done by anodisation of Si wafer in an aqueous HF with C_2H_5OH .

In this regard, anodic etching has emerged as the most widespread technique for fabricating both chip-based n- and p-type PSi. This technique makes it possible to customize the porosity and thickness of PSi required for various applications [34]. The E_f for PSi is located at the centre of the bandgap because of the decrease in the doping concentration, which is vanished through pores generation by electrochemical etching. Pores are located at Si defects and dopants [37–40]. The bandgap of the PSi is larger

than bulk Si due to the quantum confinement effect caused by reducing the crystal size for the Si nanostructure [37,41]. PSi was utilised in a solar cell to reduce the reflection (< 10%) by reducing the refractive index. But the PSi possesses two main drawbacks; (a) the PSi is oxidized after exposure to the ambient, thereby the optical properties change, (b) after surface oxidation, the recombination is improved by oxygen vacancy (shallow and deep defect) and through the surface state which names radiative state [42]. Because of these, a thin layer such as SiO₂/SiN and Al₂O₃/ SiN was utilised to passivate the PSi surface [42,43]. The PCE of the solar cell built on PSi reached 13.6%; at the graphene (GR) transparent conductive electrode (TCE)/PSi interface, graphene QDs (GQDs) [44]. The PV structure of an AuNPs/PSi/Si/Al solar cell was reported, with a 15.67% PCE [45]. The PCE of the solar cell structure of Al/Li₂O/PSi/Si/Al was 11.3% [46].

2.5.2 Mechanism of Electrochemical Etching

The mechanism of synthesised PSi, generated by electrochemical etching, relies on the type of Si. For p-type, the diffusion of holes from the Si crystal to the Si–HF interface material; electron tunnelling from the Si–HF interface to the crystal for n-type. Because a higher current density increases the number of charge carriers and thus the rate of charge exchange across the interface, the etch rate increases with current density. Figure 2.5(b) shows how an increase in substrate voltage facilitates charge exchange by lowering the energy height barrier in p-Si. Figure 2.5(d) shows how an increase in substrate voltage prevents charge exchange by increasing the energy height barrier in n-Si, which leads to generating charge tunnelling at the interface due to; an increase in the electric field and heavy doping [47–49]. On the other hand, at a high concentration of HF, the porosity of the PSi is reduced, most likely because the H⁺ ions successfully passivate the area of PSi [47,50].

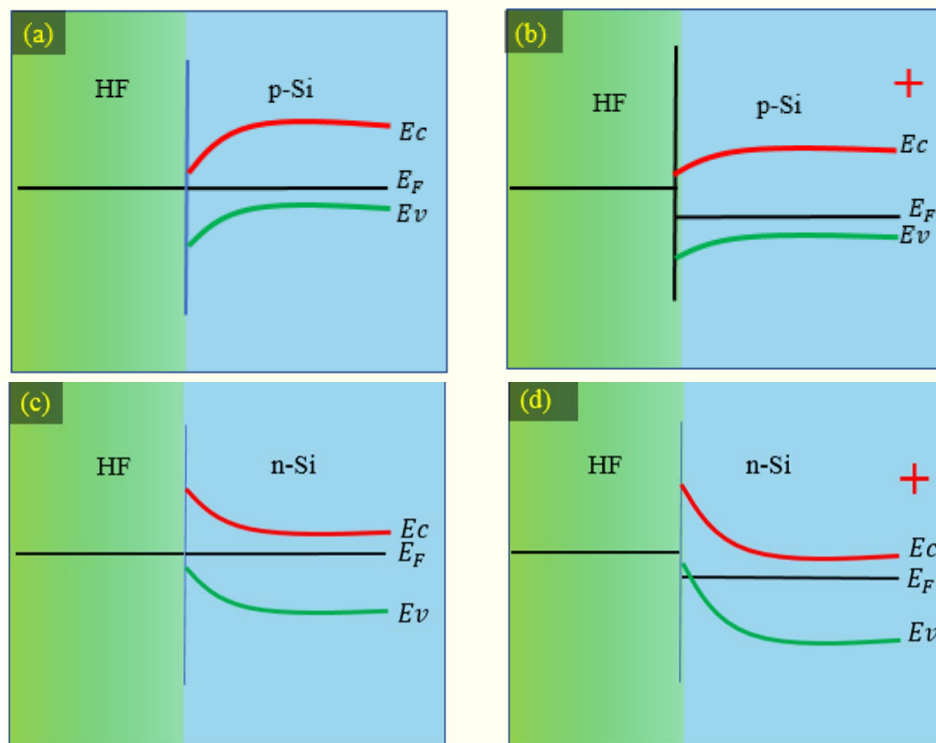


Figure 2.5 Si energy band models in HF electrolyte: (a) and (c) are p and n-Si, respectively at equilibrium condition, (b) and (d) are p and n-type Si with a positive bias voltage (+).

2.5.3 Electrochemical Etching

One of the most significant benefits of PSi is its ease of production. PSi is primarily synthesised by electrochemical dissolution of Si in HF solution. PSi cannot typically be formed by immersing the Si in an HF solution. However, in the HF solution, the current flow between two electrodes, Si at the anode and platinum (Pt) at the cathode, generates pores on the Si surface. In terms of equipment and chemicals utilised, the electrochemical etching process is a straightforward and cost-effective experimental setup [47].

PSi is formed as a result of two major factors. The first, creating SiF_2 . Second, positive mobile charge carriers are necessary for the Si anode's surface layer. The first factor is related to the electrolyte's characteristics. The second condition contributes to the significant differences in etching (p and n) type processes attributed to their

differing hole concentration. For instance, while the production of ions fluoride is essential for p-Si, it is insufficient for n-type: an external parameter activating holes generation is demand. The last parameter can be done in various ways, including heating and lighting [47].

Several studies have revealed that many parameters are involved in the formation of PSi via electrochemical etching. These parameters are as follows [47] :

- The etching current density
- The HF concentration
- The etching time
- The illumination during the etching for n-type substrates
- Si type

2.5.3(a) Etching Current Density

When it comes to determining the optical characteristics of PSi, porosity and its porous thickness are critical aspects to consider. Therefore, it is necessary to resolve the relationship between etching time and current density and the relationship between porosity and its thickness. It is discovered that increasing the current density or the etching duration increases the porosity and the porous thickness. The values of these two parameters (porosity and thickness) rise reasonably linearly with the increase in the current density; porosity is described as a percentage of the vacancy in the PSi layer and may be determined by the gravimetric method [51]. Regarding the relationship between current density and etching rate, it has been discovered that the etch rate raised proportionally with the current densities [52]. In electrochemical etching, the variation in current density impacts the dissolution process. Because the ion in the electrolyte solution is transferred, and the dissolution process occurred. When an electric field is applied to attract charge carriers, the migration of electrons and holes typically begins as the first step in the pore formation process. Si surface

chemistry is characterised by competition between the formation of Si–O, Si–F, and Si–H bonds and the construction of other bond types. When there is a high current density, it creates a strong electric field on the Si substrate. The F ions in the electrolyte were encouraged to migrate to the Si substrate, where they were reacted, resulting in dissolution, hence forming the pores. Because of the pore tip border's low potential energy compared to the wall area, the holes prefer to accumulate in bulk Si at the pore tip border [52]. It has been discovered that the current density has a more negligible effect on the pore diameter. The pore size was impacted more by the HF concentration and doping level [53].

2.5.3(b) Hydrofluoric Acid Concentration

When the concentration of HF in the electrolyte is low, and due to the lack of F ions, the oxide on the Si substrate cannot be dissolved, preventing pores from spreading [54]. According to the researchers, the rising HF concentration increases pore tip current density while minimizing the space-charge layer's width. As a result, smaller pores and a thick wall develop [54]. In addition, the dissolving Si oxide rate improves by boosting the HF volume, which immediately raises the critical current density on Si. As a result, the pore morphology grows narrow, and the thick pore barriers [54,55].

2.5.3(c) Etching Time

Because of the extended contact time between Si and the electrolyte, the porosity increases linearly with the etching duration. When etching time rises, the pore channels or the holes in the Si substrate increase, resulting in to increase in porosity [56]. The grain size becomes smaller with increasing etching time due to increased porosity. The porosity of the PSi and the peak intensity of the PL increase as the etching time increases. The rise in surface area is responsible for these patterns, as a

larger surface area contains many surface species that emit light. The porosity raises the surface roughness and reduces the carrier density because the pores are created in the defects and the doping centre [57]. Furthermore, the conductivity (σ) of a semiconductor is impacted by the energy gap, which is represented by Equation 2.3;

$$\sigma = \sigma_0 \exp\left(-\frac{E_g}{2kT}\right) \quad (2.3)$$

σ_0 is the pre-exponential factor, the Boltzmann constant is K , and the temperature is T .

Equation 2.3 demonstrates that when the energy gap widens, conductivity drops. It is referred to as an increase in the lowest energy necessary to excite an electron from the valence band to the conduction band, resulting in fewer carriers in the conduction band [58].

2.5.4 Photoluminescence of the Porous Silicon

The PL emission from the direct bandgap semiconductors (such as CdSe, PbS and Si QDs) occurs due to the radiative recombination (without phonon mediation) of the electron and hole (e^-h^+) pairs across the electronic bandgap and subsequent generation of visible photons. Conversely, the indirect bandgap semiconductors (Si and Ge) do not show visible emission due to the non-radiative recombination (with phonon mediation) of the electron and hole (e^-h^+) pairs across the electronic bandgap. The phonon assistance is required to conserve the momentum, resulting in the non-radiative recombination process. Research revealed that the indirect bandgap materials could be transformed to direct bandgap ones (breaking the momentum conservation rule) via nano-sizing. The emergent quantum confinement effect enables the materials to emit visible light of different colours depending on the size-dependent bandgap

modification [59,60]. The mechanism of the PL can be summarised as when the valance band electron is excited via a photon of energy larger than the bandgap energy, and the excited electron jumps to a higher energy state. After relaxation time, the electron recombines with a hole and emits the energy via electromagnetic waves [61].

Because it emits visible light at room temperature, PSi is one of the most promising materials. One of the essential characteristics of PSi layers is their extensive internal surface (specific surface up to $1000 \text{ m}^2/\text{cm}^3$). So one would expect that this inner surface would play an essential role in those particular PSi layer properties that differentiate from bulk material [47]. In the PL process, light is emitted spontaneously from an optically excited material, and the recorded emission spectra are used to determine its various spectroscopic parameters, such as bandgap [62]. Bulk crystalline Si does not exhibit any visible PL because of the non-radiative recombination of the carriers ($e-h$). However, at the nanoscale, the electronic energy states of Si particles smaller than the e-h exciton Bohr radius become discrete and atomic-like because of the quantum confinement effect and give rise to visible PL emission [63]. As a result, the PSi has a more significant electronic band energy gap in 1.93–1.95 eV than its bulk counterpart (1.11 eV) [62].

The approaches developed to describe the features of red PL in PSi were:

2.5.4(a) Nanosize Silicon-Established Model

Two effects must be considered when considering Si as a source for the PL at room temperature [62]:

1. The bandgap of PSi must be increased from 1.1 eV to around 1.8 eV or more.
2. PL of PSi have a high value compared to crystalline Si.

Theoretically, a band to band recombination model might explain these two effects. In the first estimate, the surface of a nanocrystallite with diameters L can be treated as an infinite potential barrier for the electronic state, with the Si dispersion integrated through the effective masses of the electrons (m_e) and holes (m_h). The practical gap energy (E_e) is then obtained by summing the Si energy bandgap and the extra energy due to confinement of the carriers, Equation 2.4:

$$E_e = E_g + \frac{\pi^2 \hbar^2}{L^2} \left(\left(\frac{1}{m_e} \right) + \left(\frac{1}{m_h} \right) \right) \quad (2.4)$$

Therefore one expects a clear $(1/L^2)$ dependence of the confinement energy on the diameters, and considerable effort has been made to reproduce this dependence experimentally both to show that the previous relationship is valid and to have the means of tuning PL energy. Using the Heisenberg uncertainty rule equation, $\Delta x \Delta p \geq \hbar$, one could explain why the PL efficiency is boosted by shrinking the particle size. The drop of Δx increases the value of Δp , and therefore Δk_x significantly induces spreading in the k space of both electron and hole states, which reduces the k selection rule [64].

2.5.4(b) Silicon Hydrogen-Established Model

These models are based on a decreased PL efficiency after hydrogen desorption using heat treatment on freshly etched PSi [65]. H is widely known for its ability to passivate Si dangling bonds. PSi that has been aged or oxidized has a low H content, with O atoms replacing the initial H atoms. Despite this, the PL is still high. The Silicon hydrogen model (SiH_x) established a model to point out that the source for PL could be found outside the Si nanocrystals. The bridge connecting the nanocrystals, in